

Learning Representations for Automatic Colorization

Gustav Larsson¹, Michael Maire², and Gregory Shakhnarovich²

¹University of Chicago ²Toyota Technological Institute at Chicago
larsson@cs.uchicago.edu, {mmaire,greg}@ttic.edu

Abstract. We develop a fully automatic image colorization system. Our approach leverages recent advances in deep networks, exploiting both low-level and semantic representations during colorization. As many scene elements naturally appear according to multimodal color distributions, we train our model to predict per-pixel color histograms. This intermediate output can be used to automatically generate a color image, or further manipulated prior to image formation; our experiments consider both scenarios. On both fully and partially automatic colorization tasks, our system significantly outperforms all existing methods.

Keywords: Automatic colorization, convolutional neural networks, hypercolumns, deep learning.



Fig. 1: Our automatic colorization of grayscale input; more examples in Figures 4 and 5.

1 Introduction

Colorization of grayscale images is a simple task for the human imagination. A human need only recall that sky is usually blue and grass is green; for many objects, the mind is free to hallucinate any of several plausible colors. The high-level comprehension required for this process is precisely why the development of fully automatic colorization algorithms remains a challenge. Colorization is therefore intriguing beyond its immediate practical utility in many graphics applications. Automatic colorization also serves as a proxy measure for visual understanding. Our work makes this connection explicit; we unify a colorization pipeline with the type of deep neural network architectures driving recent advances in image classification and object detection.

Both our technical approach and our focus on fully automatic results depart from much past work on colorization. Given its importance across multiple applications (*e.g.* historical photographs and videos [1], artist assistance [2,3]), much research strives to make colorization cheaper and less time-consuming [4–12]. However, most methods still require some level of user input [5–7,9,10,13]. Our

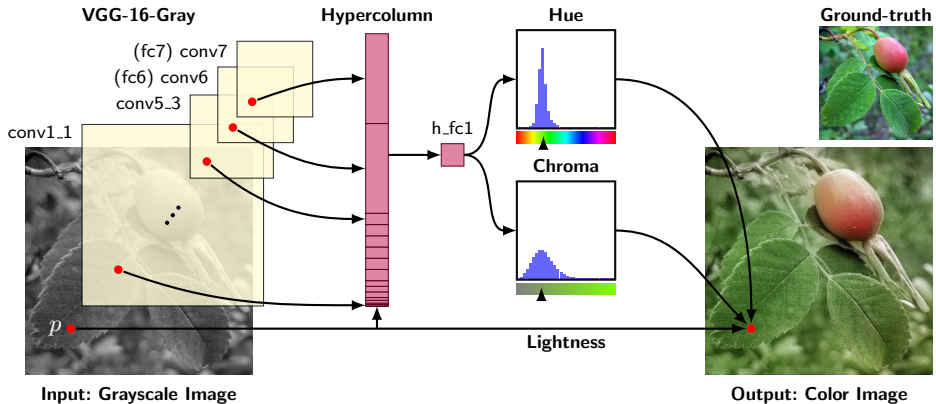


Fig. 2: **System overview.** We process a grayscale image through a deep convolutional architecture (VGG) [14] and take spatially localized multilayer slices (hypercolumns) [15–17], as per-pixel descriptors. We train our system end-to-end for the task of predicting hue and chroma distributions for each pixel p given its hypercolumn descriptor. These predicted distributions determine color assignment at test time.

work joins the relatively few recent efforts on developing fully automatic colorization algorithms [8, 11, 12]. Some [11, 12] show promising results, especially on photos of certain typical scene types (*e.g.* beaches and landscapes). However, their success is limited on complex images with foreground objects.

At a technical level, existing automatic colorization methods often employ a strategy of finding suitable reference images and transferring their color onto a target grayscale image [8, 11]. This works well if sufficiently similar reference images can be found, which becomes increasingly difficult for unique grayscale input images. Such a strategy also requires availability and search of a large repository of reference images at test time. In contrast, our approach is entirely free from database search and fast at test time. Section 2 provides a more complete view of prior methods, highlighting differences with our proposed algorithm.

Our approach to automatic colorization converts two intuitive observations into design principles. First, semantic information matters. In order to colorize arbitrary images, a system must interpret the semantic composition of the visual scene (what is in the image: faces, animals, cars, plants, ...) as well as localize scene components (where things are). Recent dramatic advances in image understanding rely on deep convolutional neural networks (CNNs) and offer tools to incorporate semantic parsing and localization into a colorization system.

Our second observation is that while some scene elements can be assigned a single color with high confidence, other elements (*e.g.* clothes or cars) may draw from many suitable colors. Thus, we design our system to predict a color histogram, instead of a single color, at every image location. Figure 2 sketches the CNN architecture we use to connect semantics with color distributions by exploiting features across multiple abstraction levels. Section 3 provides details.

Section 4 reports extensive experimental validation of our algorithm against competing methods [4, 11] in two settings: fully (grayscale input only) and par-

tially (grayscale input and reference global color histogram provided) automatic colorization. Across every benchmark metric and every dataset [18–20], our method achieves the best performance. Lacking an established standard colorization benchmark, exhaustive comparison is necessary. To ease this burden for future research, we propose a new colorization benchmark on the ImageNet dataset [20], which may simplify quantitative comparisons and drive further progress. Our system achieves such a drastic performance leap that its fully automatic colorization output is superior to that of prior methods relying on additional information such as reference images or ground-truth color histograms.

Section 5 summarizes our contributions: (1) a novel technical approach to colorization, bringing semantic knowledge to bear using CNNs, and modeling color distributions; (2) state-of-the-art performance across fully and partially automatic colorization tasks; (3) a new ImageNet colorization benchmark.

2 Related work

Previous colorization methods broadly fall into three categories: scribble-based [3, 5, 21–23], transfer-based [4, 6–10, 24], and automatic direct prediction [11, 12].

Scribble-based methods, introduced by Levin *et al.* [5], require manually specifying desired colors of certain regions. These scribble colors are propagated under the assumption that adjacent pixels with similar luminance should have similar color, with the optimization relying on Normalized Cuts [25]. Users can interactively refine results by providing additional scribbles. Further advances within this family of methods extend the notion of similarity to texture [3, 23], and exploit edges to reduce color bleeding [21].

Transfer-based methods rely on availability of related *reference* image(s), from which color is transferred to the target grayscale image. Mapping between source and target is established automatically, using correspondences between local descriptors [4, 7, 8], or in combination with manual intervention [6, 9]. Excepting [8], reference image selection is at least partially manual.

In contrast to these method families, our goal is *fully automatic* colorization. We are aware of two recent efforts in this direction. Deshpande *et al.* [11] colorize an entire image by solving a linear system. This can be seen as an extension of patch-matching techniques [4], adding interaction terms for spatial consistency. Regression trees address the high-dimensionality of the system. Inference requires an iterative algorithm. Most of the experiments are focused on a dataset (SUN-6) limited to images of a few scene classes, and best results are obtained when the scene class is known at test time. They also examine another partially automatic task, in which a desired global color histogram is provided.

The work of Cheng *et al.* [12] is perhaps most related to ours. It combines three levels of features with increasing receptive field: the raw image patch, DAISY features [26], and semantic features [27]. These features are concatenated and fed into a three-layer fully connected neural network trained with an L_2 loss. Only this last component is optimized; the feature representations are fixed.

Unlike [11] and [12], our system does not rely on hand-crafted features, is trained end-to-end, and treats color prediction as a histogram estimation task rather than as regression. Experiments in Section 4 justify these principles by demonstrating performance superior to the best reported by [11, 12] across all regimes. But first, we elaborate the specifics of our architecture and algorithm.

3 Method

We frame the colorization problem as learning a function $f : \mathcal{X} \rightarrow \mathcal{Y}$. Given a grayscale image patch $\mathbf{x} \in \mathcal{X} = [0, 1]^{S \times S}$, f predicts the color $\mathbf{y} \in \mathcal{Y}$ of its center pixel. The patch size $S \times S$ is the receptive field of the colorizer. The output space \mathcal{Y} depends on the choice of color parameterization. We implement f according to the neural network architecture diagrammed in Figure 2.

Motivating this strategy is the success of similar architectures for semantic segmentation [16, 17, 27–29] and boundary detection [15, 30–33]. Together with colorization, these tasks can all be viewed as image-to-image prediction problems, in which a value is predicted for each input pixel. Leading methods commonly adapt deep convolutional neural networks pretrained for image classification [14, 20]. Such classification networks can be converted to *fully convolutional* networks that produce output of the same spatial size as the input, *e.g.* using the shift-and-stitch method [27] or the more efficient *à trous* algorithm [29]. Subsequent training with a task-specific loss fine-tunes the converted network.

Skip-layer connections, which directly link low- and mid-level features to prediction layers, are an architectural addition beneficial for many image-to-image problems. Some methods implement skip connections directly through concatenation layers [27, 29], while others equivalently extract per-pixel descriptors by reading localized slices of multiple layers [15–17]. We use this latter strategy and adopt the recently coined *hypercolumn* terminology [17] for such slices.

Though we build upon these ideas, our technical approach innovates on two fronts. First, we integrate domain knowledge for colorization, experimenting with output spaces and loss functions. We design the network output to serve as an intermediate representation, appropriate for direct or biased sampling. We introduce an energy minimization procedure for optionally biasing sampling towards a reference image. Second, we develop a novel and efficient computational strategy for network training that is widely applicable to hypercolumn architectures.

3.1 Color spaces

We generate training data by converting color images to grayscale according to $L = \frac{R+G+B}{3}$. This is only one of many desaturation options and chosen primarily to facilitate comparison with Deshpande *et al.* [11]. For the representation of color predictions, using RGB is overdetermined, as lightness L is already known. We instead consider output color spaces with L (or a closely related quantity) conveniently appearing as a separate pass-through channel:

- **Hue/chroma.** Hue-based spaces, such as HSL, can be thought of as a color cylinder, with angular coordinate H (hue), radial distance S (saturation), and height L (lightness). The color is constant with respect to S and H at the bottom (black) and top (white) of the cylinder, making S and H arbitrary (and thus unstable) close to those regions. HSV describes a similar color cylinder which is only unstable at the bottom. However, L is no longer one of the channels. We wish to avoid both instabilities and still retain L as a channel. The solution is a color bicone, where chroma (C) takes the place of saturation. This color space only has instability in H around $C = 0$; this is inherent to all hue-based color spaces and we show how to overcome this when designing the loss function. Conversion to HSV is given by $V = L + \frac{C}{2}$, $S = \frac{C}{V}$.
- **Lab and $\alpha\beta$.** Lab (or L*a*b) is designed to be perceptually linear. The color vector (a, b) defines a Euclidean space where the distance to the origin determines chroma. Deshpande *et al.* [11] use a color space somewhat similar to Lab, denoted “ab”. To differentiate, we call their color space $\alpha\beta$.

3.2 Loss

For any output color representation, we require a loss function for measuring prediction errors. A first consideration, also used in [12], is L_2 regression in Lab:

$$L_{\text{reg}}(\mathbf{x}, \mathbf{y}) = \|f(\mathbf{x}) - \mathbf{y}\|^2 \quad (1)$$

where $\mathcal{Y} = \mathbb{R}^2$ describes the (a, b) vector space. However, regression targets do not handle multimodal color distributions well. To address this, we instead predict distributions over a set of color bins, a technique also used in [7]:

$$L_{\text{hist}}(\mathbf{x}, \mathbf{y}) = D_{\text{KL}}(\mathbf{y} \| f(\mathbf{x})) \quad (2)$$

where $\mathcal{Y} = [0, 1]^K$ describes a histogram over K bins, and D_{KL} is the KL-divergence. The ground-truth histogram \mathbf{y} is set as the empirical distribution in a rectangular region of size R around the center pixel. Somewhat surprisingly, our experiments see no benefit to predicting smoothed histograms, so we simply set $R = 1$. This makes \mathbf{y} a one-hot vector and Equation (2) the log loss. For histogram predictions, the last layer of neural network f is always a softmax.

There are several choices of how to bin color space. We bin the Lab axes by evenly spaced Gaussian quantiles ($\mu = 0, \sigma = 25$). They can be encoded separately for a and b (as marginal distributions), in which case our loss becomes the sum of two separate terms defined by Equation (2). They can also be encoded as a joint distribution over a and b , in which case we let the quantiles form a 2D grid of bins. In our experiments, we set $K = 32$ for marginal distributions and $K = 16 \times 16$ for joint. We determined these numbers, along with σ , to offer a good compromise of output fidelity and output complexity.

For hue/chroma, we only consider marginal distributions and bin axes uniformly in $[0, 1]$. Since hue becomes unstable as chroma approaches zero, we add

a sample weight to the hue based on the chroma:

$$L_{\text{hue/chroma}}(\mathbf{x}, \mathbf{y}) = D_{\text{KL}}(\mathbf{y}_C \| f_C(\mathbf{x})) + \lambda_H y_C D_{\text{KL}}(\mathbf{y}_H \| f_H(\mathbf{x})) \quad (3)$$

where $\mathcal{Y} = [0, 1]^{2 \times K}$, and $y_C \in [0, 1]$ is the chroma value at the sample pixel. We set $\lambda_H = 5$, which is roughly the inverse expectation of y_C , so that hue and chroma are equally weighted.

3.3 Inference

Given network f trained according to a loss function in the previous section, we evaluate it at every pixel n in a test image: $\hat{\mathbf{y}}_n = f(\mathbf{x}_n)$. For the L_2 loss, all that remains is to combine each $\hat{\mathbf{y}}_n$ with the respective input lightness and convert to RGB. However, when the predictions are histograms, we must infer a final color. We consider several options:

- **Sample** Draw a sample from the histogram. If done per pixel, this may create high-frequency color changes in areas of high-entropy histograms.
- **Mode** Take the $\arg \max_k \hat{y}_{n,k}$ as the color. This can create jarring transitions between colors, and is prone to vote splitting when two or more bins have proximal centroids.
- **Median** Compute cumulative sum of $\hat{\mathbf{y}}_n$ and use linear interpolation to find the value at the middle bin. Undefined for circular histograms, such as hue.
- **Expectation** Sum over the color bin centroids weighted by the histogram.

For Lab output, we achieve the best qualitative and quantitative results using expectations. For hue/chroma, the best results are achieved by taking the median of the chroma. Many objects can appear both with and without chroma, which means $C = 0$ is a particularly common bin. This mode draws the expectation closer to zero, producing less saturated images. As for hue, since it is circular, we first compute the complex expectation:

$$z = \mathbb{E}_{H \sim f_h(\mathbf{x})}[H] \triangleq \frac{1}{K} \sum_k [f_h(x)]_k e^{i\theta_k}, \quad \theta_k = 2\pi \frac{k + 0.5}{K} \quad (4)$$

We then set hue to the argument of z remapped to lie in $[0, 1)$.

In cases where the estimate of the chroma is high and z is close to zero, the instability of the hue can create artifacts (Figure 3). A simple, yet effective, fix is chromatic fading: downweight the chroma if the absolute value of z is too small. We thus re-define the predicted chroma as:

$$C_{\text{faded}} = \max(\eta^{-1}|z|, 1) \cdot C \quad (5)$$

In our experiments, we set $\eta = 0.03$ (obtained via cross-validation).



Fig. 3: Artifacts without chromatic fading (*left*).

3.4 Histogram transfer from ground-truth

So far, we have only considered the fully automatic color inference task. Deshpande *et al.* [11], test a separate task where the ground-truth histogram in the two non-lightness color channels of the original color image is made available.¹ In order to compare, we propose two histogram transfer methods. We refer to the predicted image as the *source* and the ground-truth image as the *target*.

Lightness-normalized quantile matching. Take the RGB representation of both the source and the target and divide by their respective lightness L . Compute marginal histograms over the three resulting color channels. Alter each source histogram to fit the corresponding target histogram by quantile matching. Multiply the resulting image by L . This quantile matching is surprisingly effective and beats the cluster correspondence method proposed in [11] (see Table 3). However, it does not exploit our richer predictions of color distributions.

Energy minimization. We phrase histogram matching as minimizing energy:

$$E = \frac{1}{N} \sum_n D_{\text{KL}}(\hat{\mathbf{y}}_n^* \|\hat{\mathbf{y}}_n) + \lambda D_{\chi^2}(\langle \hat{\mathbf{y}}^* \rangle, \mathbf{t}) \quad (6)$$

where N is the number of pixels, $\hat{\mathbf{y}}, \hat{\mathbf{y}}^* \in [0, 1]^{N \times K}$ are the predicted and posterior distributions, respectively. The target histogram is denoted by $\mathbf{t} \in [0, 1]^K$. The first term contains unary potentials that anchor the posteriors to the predictions. The second term is a symmetric χ^2 distance to promote proximity between source and target histograms. Weight λ defines relative importance of histogram matching. We estimate the source histogram as $\langle \hat{\mathbf{y}}^* \rangle = \frac{1}{N} \sum_n \hat{\mathbf{y}}_n^*$. We parameterize the posterior for all pixels n as: $\hat{\mathbf{y}}_n^* = \text{softmax}(\log \hat{\mathbf{y}}_n + \mathbf{b})$, where the vector $\mathbf{b} \in \mathbb{R}^K$ can be seen as a global bias for each bin. It is also possible to solve for the posteriors directly; this does not perform better quantitatively and is more prone to introducing artifacts. We solve for \mathbf{b} using gradient descent on E and use the resulting posteriors in place of the predictions. In the case of marginal histograms, the optimization is run twice, once for each color channel.

3.5 Neural network architecture and training

Our base network is a fully convolutional version of VGG-16 [14] with two changes: (1) the classification layer (`fc8`) is discarded, and (2) the first filter layer (`conv1_1`) operates on a single intensity channel instead of mean-subtracted RGB. We extract a hypercolumn descriptor for a pixel by concatenating the features at its spatial location in all layers, from `data` to `conv7` (`fc7`), resulting in a 12,417 channel descriptor. We feed this hypercolumn into a fully connected layer with 1024 channels (`h_fc1` in Figure 2), to which we connect output predictors.

¹ Note that if the histogram of the L channel were available, it would be possible to match lightness to lightness exactly and thus greatly narrow down color placement.

Processing each pixel separately in such manner would be extremely costly. We can instead run an entire image through a single forward pass of VGG-16 and approximate the hypercolumns using bilinear interpolation. Even with such sharing, extracting hypercolumns densely over the entire image requires upsampling each layer to the same spatial size. For a 256×256 input image, the hypercolumns alone require significant memory (1.7 GB).

To fit image batches in memory during training, we instead extract hypercolumns at only a sparse set of locations, implementing a custom Caffe [34] layer to directly compute them.² Extracting batches of only 128 hypercolumn descriptors per input image, sampled at random locations, provides sufficient training signal. In the backward pass of stochastic gradient descent, an interpolated hypercolumn propagates its gradients to the four closest spatial cells in each layer. We ensure atomicity of gradient updates using locks, without incurring any performance penalty. This strategy drops training memory usage for hypercolumns to only 13 MB per image.

We initialize with a version of VGG-16 pretrained on ImageNet, adapting it to grayscale by averaging over color channels in the first layer and rescaling appropriately. Prior to training for colorization, we further fine-tune the network for one epoch on the ImageNet classification task with grayscale input. As the original VGG-16 was trained without batch normalization [35], scale of responses in internal layers can vary dramatically, presenting a problem for learning atop their hypercolumn concatenation. Liu *et al.* [36] compensate for such variability by applying layer-wise L_2 normalization. We use the alternative of balancing hypercolumns so that each layer has roughly unit second moment ($\mathbb{E}[X^2] \approx 1$); additional details are provided in the Appendix (Section A.1).

4 Experiments

Starting from pretrained VGG-16-Gray, described in the previous section, we attach **h_fc1** and output prediction layers with Xavier initialization [37], and fine-tune the entire system for colorization. We consider multiple prediction layer variants: Lab output with L_2 loss, and both Lab and hue/chroma marginal or joint histogram output with losses according to Equations (2) and (3). We train each system variant end-to-end for one epoch on the 1.2 million images of the ImageNet training set, each resized to at most 256 pixels in smaller dimension. A single epoch takes approximately 17 hours on an NVIDIA Titan X GPU. At test time, colorizing a single 512×512 pixel image takes 0.5 seconds.

We setup two disjoint subsets of the ImageNet validation data for our own use: 1000 validation images (**cval1k**) and 10000 test images (**ctest10k**). Each set has a balanced representation for ImageNet categories, and excludes any images encoded as grayscale, but may include images that are naturally grayscale (*e.g.* closeup of nuts and bolts), where an algorithm should know not to add color. Category labels are discarded; only images are available at test time. We propose **ctest10k** as a standard benchmark with the following metrics:

² We will make all code and trained models public soon.

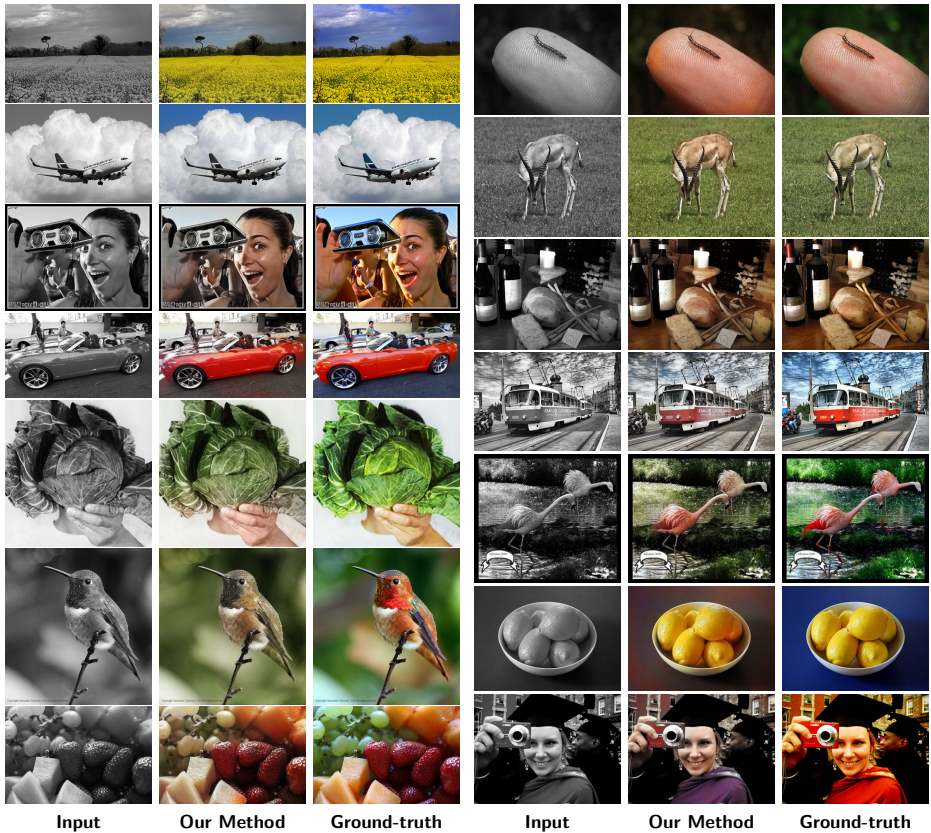


Fig. 4: **Fully automatic colorization results on ImageNet/ctest10k.** Our system reproduces known object color properties (e.g. faces, sky, grass, fruit, wood), and coherently picks colors for objects without such properties (e.g. clothing).

Model\Metric	RMSE	PSNR
No colorization	0.343	22.98
Lab, L_2	0.318	24.25
Lab, $K = 32$	0.321	24.33
Lab, $K = 16 \times 16$	0.328	24.30
Hue/chroma, $K = 32$	0.342	23.77
+ chromatic fading	0.299	24.45

Table 1: **ImageNet/cval1k.** Validation performance of system variants. Hue/chroma is best, but only with chromatic fading.

Model\Metric	RMSE	PSNR
data..fc7	0.299	24.45
data..conv5.3	0.306	24.13
conv4.1..fc7	0.302	24.45
conv5.1..fc7	0.307	24.38
fc6..fc7	0.323	24.22
fc7	0.324	24.19

Table 2: **ImageNet/cval1k.** Ablation study of hypercolumn components.

- **RMSE**: root mean square error in $\alpha\beta$ averaged over all pixels [11].
- **PSNR**: peak signal-to-noise ratio in RGB calculated per image [12]. We use the arithmetic mean of PSNR over images, instead of the geometric mean as in Cheng *et al.* [12]; geometric mean is overly sensitive to outliers.



Fig. 5: **Additional results.** *Top:* Our automatic colorizations of these ImageNet examples are difficult to distinguish from real color images. *Bottom:* B&W photographs.

By virtue of comparing to ground-truth color images, quantitative colorization metrics can penalize reasonable, but incorrect, color guesses for many objects (*e.g.* red car instead of blue car) more than jarring artifacts. This makes qualitative results for colorization as important as quantitative; we report both.

Figures 1, 4, and 5 show example test results of our best system variant, selected according to performance on the validation set and trained for a total

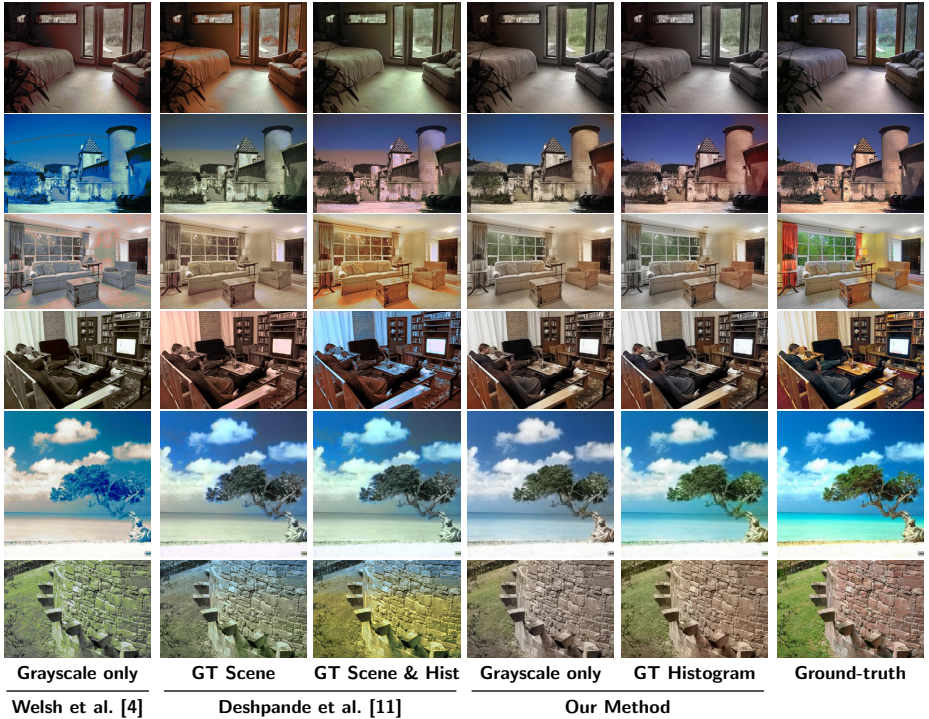


Fig. 6: **Comparison with leading methods on SUN-6.** GT Scene: test image scene class is available. GT Hist: test image color histogram is available. We obtain colorizations with visual quality better than those from prior work, even though we do not exploit reference images or known scene class. Using our energy minimization transfer method (Section 3.4) when GT Hist is available further improves results. In either mode, our method appears less dependent on spatial priors: note splitting of the sky in the second row and correlation of green with actual grass in the last row.

of 10 epochs. This variant predicts hue and chroma and uses chromatic fading during image generation. Table 1 provides complete validation benchmarks for all system variants, including the trivial baseline of no colorization (returning the grayscale input). On ImageNet test (**ctest10k**), our selected model obtains 0.293 (RMSE, $\alpha\beta$, avg/px) and 24.94 dB (PSNR, RGB, avg/im), compared to 0.333 and 23.27 dB for the no colorization baseline.

Table 2 examines the importance of different neural network layers to colorization; it reports validation performance of ablated systems that include only the specified subsets of layers in the hypercolumn used to predict hue and chroma. Some lower layers may be discarded without much performance loss, yet higher layers alone (**fc6..fc7**) are insufficient for good colorization.

Our ImageNet colorization benchmark is new to a field lacking an established evaluation protocol. We therefore focus on comparisons with two recent papers [11, 12], using their self-defined evaluation criteria. To do so, we run our ImageNet-trained hue and chroma model on two additional datasets:

Method	RMSE
Grayscale (no colorization)	0.285
Welsh <i>et al.</i> [4]	0.353
Deshpande <i>et al.</i> [11]	0.262
+ GT Scene	0.254
Our Method	0.211

Table 3: **SUN-6**. Comparison with competing methods.

Method	RMSE
Deshpande <i>et al.</i> (C) [11]	0.236
Deshpande <i>et al.</i> (Q)	0.211
Our Method (Q)	0.178
Our Method (E)	0.165

Table 4: **SUN-6 (GT Hist)**. Comparison using ground-truth histograms. Results for Deshpande *et al.* [11] use GT Scene.

- **SUN-A** [19] is a subset of the SUN dataset [18] containing 47 object categories. Cheng *et al.* [12] train a colorization system on 2688 images and report results on 1344 test images. We were unable to obtain the list of test images, and therefore report results averaged over five random subsets of 1344 SUN-A images. We do not use any SUN-A images for training.
- **SUN-6**, another SUN subset, used by Deshpande *et al.* [11], includes images from 6 scene categories (beach, castle, outdoor, kitchen, living room, bedroom). We compare our results on 240 test images to those reported in [11] for their method as well as for Welsh *et al.* [4] with automatically matched reference images as in [8]. Following [11], we consider another evaluation regime in which ground-truth target color histograms are available.

Figure 6 shows a comparison of results on SUN-6. Forgoing usage of ground-truth global histograms, our fully automatic system produces output qualitatively superior to methods relying on such side information. Tables 3 and 4 report quantitative performance corroborating this view. The partially automatic systems in Table 4 adapt output to fit global histograms using either: (C) cluster correspondences [11], (Q) quantile matching, or (E) our energy minimization de-

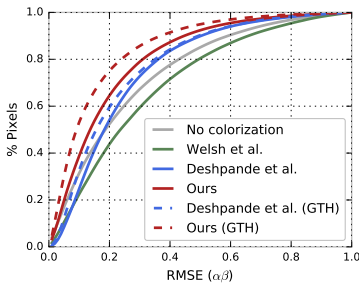


Fig. 7: **SUN-6**. Cumulative histogram of per pixel error (higher=more pixels with lower error). Results for Deshpande *et al.* [11] use GT Scene.

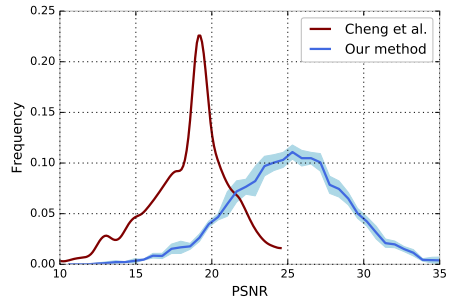


Fig. 8: **SUN-A**. Histogram of per-image PSNR for [12] and our method. The highest geometric mean PSNR reported for experiments in [12] is 24.2, vs. **32.7±2.0** for us.

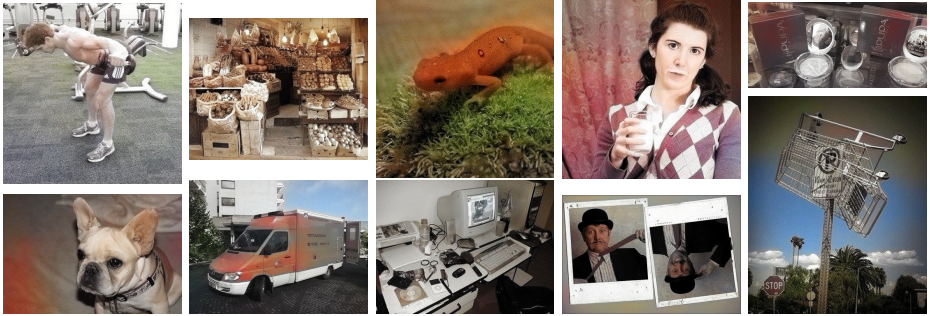


Fig. 9: **Failure modes.** *Top row, left-to-right:* texture confusion, too homogeneous, color bleeding, unnatural color shifts ($\times 2$). *Bottom row:* inconsistent background, inconsistent chromaticity, not enough color, object not recognized (upside down face partly gray), context confusion (sky).

scribed in Section 3.4. Our quantile matching results are superior to those of [11] and our new energy minimization procedure offers further improvement.

Figures 7 and 8 compare error distributions on SUN-6 and SUN-A. As in Table 3, our fully automatic method dominates all competing approaches, even those which use auxiliary information. It is only outperformed by the version of itself augmented with ground-truth global histograms. On SUN-A, Figure 8 shows clear separation between our method and [12] on per-image PSNR.

The Appendix (Figures 13 and 14) provides anecdotal comparisons to one additional method, that of Charpiat *et al.* [38], which can be considered an automatic system if reference images are available. Unfortunately, source code of [38] is not available and reported time cost is prohibitive for large-scale evaluation (30 minutes per image). We were thus unable to benchmark [38] on large datasets.

Though we achieve significant improvements compared to the state-of-the-art, our results are not perfect. Figure 9 shows examples of significant failures. Minor imperfections can also be seen in some of the successful colorization results in Figures 4 and 5. We believe a common failure mode may correlate with gaps in semantic interpretation: incorrectly identified or unfamiliar objects and incorrect segmentation. In addition, there are “mistakes” due to natural uncertainty of color – *e.g.* the graduation robe at the bottom right of Figure 4 is red, but could as well be purple.

Since our method produces histograms, we can provide an interactive means of biasing uncertain colorizations according to user input preferences. Rather than output a single color per pixel, we can sample color for image regions, driven by the predicted histograms, and evaluate color uncertainty.

Specifically, solving our energy minimization formulation (Equation (6)) with global biases \mathbf{b} that are not optimized based on a reference image, but simply “rotated” through color space, induces changed color preferences everywhere in the image. The effect is modulated by the uncertainty in the predicted color histogram. Figure 10 shows multiple sampled colorizations, together with a vi-



Fig. 10: **Sampling multiple colorizations.** From left: graylevel input; three colorizations sampled from our model; color uncertainty map according to our model.

sualization of color uncertainty. Here, we calculate uncertainty as the entropy of the predicted hue multiplied by the chroma.

We believe our distributional output representation and energy minimization framework open the path for future investigation of interactive human-in-the-loop colorization tools.

5 Conclusion

We present a system that demonstrates state-of-the-art ability to automatically colorize grayscale images. Two novel contributions enable this progress: a deep neural architecture that is trained end-to-end to incorporate semantically meaningful features of varying complexity into colorization, and a color histogram prediction framework that handles uncertainty and ambiguities inherent in colorization while preventing jarring artifacts. Our fully automatic colorizer produces strong results, improving upon previously leading methods by large margins on all datasets tested; we also propose a new large-scale generic benchmark for automatic image colorization, and establish a strong baseline with our method to facilitate future comparisons. Our colorization results are visually appealing even on complex scenes, and allow for effective post-processing with creative control via color histogram transfer and intelligent, uncertainty-driven color sampling.

6 Acknowledgements

We would like to thank Ayan Chakrabarti for suggesting the lightness-normalized quantile matching method and for useful discussions, and Aditya Deshpande and Jason Rock for a helpful discussion on colorization and on their work. We gratefully acknowledge the support of NVIDIA Corporation with the donation of GPUs used for this research.

References

1. Tsafaris, S.A., Casadio, F., Andral, J.L., Katsaggelos, A.K.: A novel visualization tool for art history and conservation: Automated colorization of black and white archival photographs of works of art. *Studies in Conservation* **59**(3) (2014)
2. Šýkora, D., Buriánek, J., Žára, J.: Unsupervised colorization of black-and-white cartoons. In: *International symposium on Non-photorealistic animation and rendering*. (2004)
3. Qu, Y., Wong, T.T., Heng, P.A.: Manga colorization. *ACM Transactions on Graphics (TOG)* **25**(3) (2006)
4. Welsh, T., Ashikhmin, M., Mueller, K.: Transferring color to greyscale images. *ACM Transactions on Graphics (TOG)* **21**(3) (2002)
5. Levin, A., Lischinski, D., Weiss, Y.: Colorization using optimization. *ACM Transactions on Graphics (TOG)* **23**(3) (2004)
6. Irony, R., Cohen-Or, D., Lischinski, D.: Colorization by example. In: *Eurographics Symp. on Rendering*. (2005)
7. Charpiat, G., Hofmann, M., Schölkopf, B.: Automatic image colorization via multimodal predictions. In: *ECCV*. (2008)
8. Morimoto, Y., Taguchi, Y., Naemura, T.: Automatic colorization of grayscale images using multiple images on the web. In: *SIGGRAPH: Posters*. (2009)
9. Chia, A.Y.S., Zhuo, S., Gupta, R.K., Tai, Y.W., Cho, S.Y., Tan, P., Lin, S.: Semantic colorization with internet images. *ACM Transactions on Graphics (TOG)* **30**(6) (2011)
10. Gupta, R.K., Chia, A.Y.S., Rajan, D., Ng, E.S., Zhiyong, H.: Image colorization using similar images. In: *ACM international conference on Multimedia*. (2012)
11. Deshpande, A., Rock, J., Forsyth, D.: Learning large-scale automatic image colorization. In: *ICCV*. (2015)
12. Cheng, Z., Yang, Q., Sheng, B.: Deep colorization. In: *ICCV*. (2015)
13. Sapiro, G.: Inpainting the colors. In: *ICIP*. (2005)
14. Simonyan, K., Zisserman, A.: Very deep convolutional networks for large-scale image recognition. In: *ICLR*. (2015)
15. Maire, M., Yu, S.X., Perona, P.: Reconstructive sparse code transfer for contour detection and semantic labeling. In: *ACCV*. (2014)
16. Mostajabi, M., Yadollahpour, P., Shakhnarovich, G.: Feedforward semantic segmentation with zoom-out features. In: *CVPR*. (2015)
17. Hariharan, B., Girshick, P.A., Malik, J.: Hypercolumns for object segmentation and fine-grained localization. *CVPR* (2015)
18. Xiao, J., Hays, J., Ehinger, K.A., Oliva, A., Torralba, A.: Sun database: Large-scale scene recognition from abbey to zoo. In: *CVPR*. (2010)

19. Patterson, G., Xu, C., Su, H., Hays, J.: The sun attribute database: Beyond categories for deeper scene understanding. *International Journal of Computer Vision* **108**(1-2) (2014)
20. Russakovsky, O., Deng, J., Su, H., Krause, J., Satheesh, S., Ma, S., Huang, Z., Karpathy, A., Khosla, A., Bernstein, M., Berg, A.C., Fei-Fei, L.: ImageNet Large Scale Visual Recognition Challenge. *International Journal of Computer Vision (IJCV)* **115**(3) (2015)
21. Huang, Y.C., Tung, Y.S., Chen, J.C., Wang, S.W., Wu, J.L.: An adaptive edge detection based colorization algorithm and its applications. In: ACM international conference on Multimedia. (2005)
22. Yatziv, L., Sapiro, G.: Fast image and video colorization using chrominance blending. *Image Processing, IEEE Transactions on* **15**(5) (2006)
23. Luan, Q., Wen, F., Cohen-Or, D., Liang, L., Xu, Y.Q., Shum, H.Y.: Natural image colorization. In: Eurographics conference on Rendering Techniques. (2007)
24. Tai, Y.W., Jia, J., Tang, C.K.: Local color transfer via probabilistic segmentation by expectation-maximization. In: CVPR. (2005)
25. Shi, J., Malik, J.: Normalized cuts and image segmentation. *Pattern Analysis and Machine Intelligence, IEEE Transactions on* **22**(8) (2000)
26. Tola, E., Lepetit, V., Fua, P.: A fast local descriptor for dense matching. In: CVPR. (2008)
27. Long, J., Shelhamer, E., Darrell, T.: Fully convolutional networks for semantic segmentation. In: CVPR. (2015)
28. Farabet, C., Couprie, C., Najman, L., LeCun, Y.: Learning hierarchical features for scene labeling. *Pattern Analysis and Machine Intelligence, IEEE Transactions on* **35**(8) (2013)
29. Chen, L.C., Papandreou, G., Kokkinos, I., Murphy, K., Yuille, A.L.: Semantic image segmentation with deep convolutional nets and fully connected crfs. In: ICLR. (2015)
30. Ganin, Y., Lempitsky, V.S.: N^4 -fields: Neural network nearest neighbor fields for image transforms. In: ACCV. (2014)
31. Bertasius, G., Shi, J., Torresani, L.: Deepedge: A multi-scale bifurcated deep network for top-down contour detection. In: CVPR. (2015)
32. Shen, W., Wang, X., Wang, Y., Bai, X., Zhang, Z.: Deepcontour: A deep convolutional feature learned by positive-sharing loss for contour detection. In: CVPR. (2015)
33. Xie, S., Tu, Z.: Holistically-nested edge detection. In: ICCV. (2015)
34. Jia, Y., Shelhamer, E., Donahue, J., Karayev, S., Long, J., Girshick, R., Guadarrama, S., Darrell, T.: Caffe: Convolutional architecture for fast feature embedding. *arXiv preprint arXiv:1408.5093* (2014)
35. Ioffe, S., Szegedy, C.: Batch normalization: Accelerating deep network training by reducing internal covariate shift. In: ICML. (2015)
36. Liu, W., Rabinovich, A., Berg, A.C.: Parsenet: Looking wider to see better. *arXiv preprint arXiv:1506.04579* (2015)
37. Glorot, X., Bengio, Y.: Understanding the difficulty of training deep feedforward neural networks. In: AISTATS. (2010)
38. Charpiat, G., Bezrukov, I., Altun, Y., Hofmann, M., Schölkopf, B.: Machine learning methods for automatic image colorization. In: *Computational Photography: Methods and Applications*. CRC Press (2010)

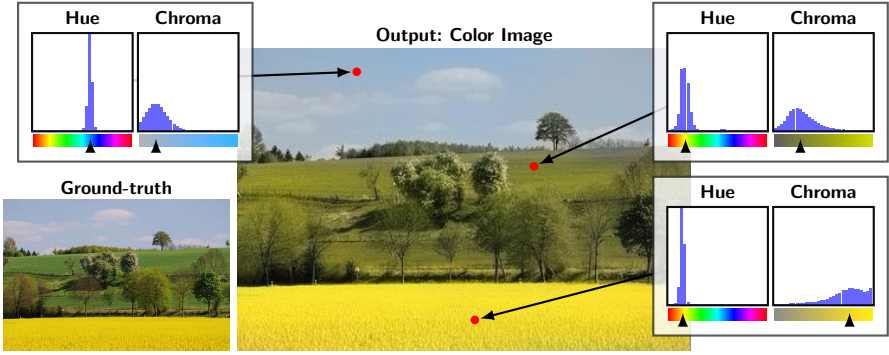


Fig.11: **Histogram predictions.** Example of predicted hue/chroma histograms.

Appendix A provides additional training and evaluation details. This is followed by more results and examples in Appendix B.

A Supplementary details

A.1 Re-balancing

To adjust the scale of the activations of layer l by factor m , without changing any other layer’s activation, the weights \mathbf{W} and the bias \mathbf{b} are updated according to:

$$\mathbf{W}_l \leftarrow m\mathbf{W}_l \quad \mathbf{b}_l \leftarrow m\mathbf{b}_l \quad \mathbf{W}_{l+1} \leftarrow \frac{1}{m}\mathbf{W}_{l+1} \quad (7)$$

The activation of \mathbf{x}_{l+1} becomes:

$$\mathbf{x}_{l+1} = \frac{1}{m}\mathbf{W}_{l+1}\text{ReLU}(m\mathbf{W}_l\mathbf{x}_l + m\mathbf{b}_l) + \mathbf{b}_{l+1} \quad (8)$$

The m inside the ReLU will not affect whether or not a value is rectified, so the two cases remain the same: (1) negative: the activation will be the corresponding feature in \mathbf{b}_{l+1} regardless of m , and (2) positive: the ReLU becomes the identity function and m and $\frac{1}{m}$ cancel to get back the original activation.

We set $m = \frac{1}{\sqrt{\mathbb{E}[X^2]}}$, estimated for each layer separately.

A.2 Color space $\alpha\beta$

The color channels $\alpha\beta$ (“ab” in [11]) are calculated as

$$\alpha = \frac{B - \frac{1}{2}(R + G)}{L + \epsilon} \quad \beta = \frac{R - G}{L + \epsilon} \quad (9)$$

where $\epsilon = 0.0001$, $R, G, B \in [0, 1]$ and $L = \frac{R+G+B}{3}$.³

³ We know that this is how Deshpande *et al.* [11] calculate it based on their code release.

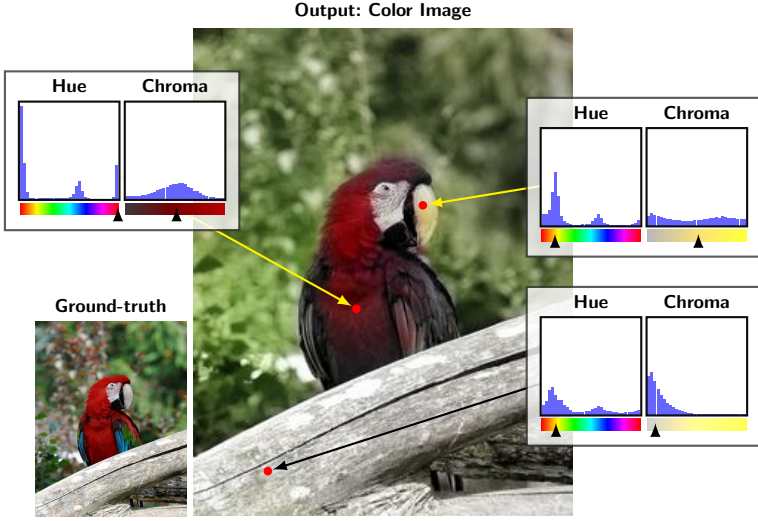


Fig.12: **Histogram predictions.** Example of predicted hue/chroma histograms.

A.3 Error metrics

For M images, each image m with N_m pixels, we calculate the error metrics as:

$$\text{RMSE} = \frac{1}{\sum_{m=1}^M N_m} \sum_{m=1}^M \sum_{n=1}^{N_m} \sqrt{\left\| \left[\mathbf{y}_{\alpha\beta}^{(m)} \right]_n - \left[\hat{\mathbf{y}}_{\alpha\beta}^{(m)} \right]_n \right\|^2} \quad (10)$$

$$\text{PSNR} = \frac{1}{M} \sum_{m=1}^M \sum_{n=1}^{N_m} -10 \cdot \log_{10} \left(\frac{\left\| \mathbf{y}_{\text{RGB}}^{(m)} - \hat{\mathbf{y}}_{\text{RGB}}^{(m)} \right\|^2}{3N_m} \right) \quad (11)$$

Where $\mathbf{y}_{\alpha\beta}^{(m)} \in [-3, 3]^{N_m \times 2}$ and $\mathbf{y}_{\text{RGB}}^{(m)} \in [0, 1]^{N_m \times 3}$ for all m .

A.4 Lightness correction

Ideally the lightness L is an unaltered pass-through channel. However, due to subtle differences in how L is defined, it is possible that the lightness of the predicted image, \hat{L} , does not agree with the input, L . To compensate for this, we add $L - \hat{L}$ to all color channels in the predicted RGB image as a final corrective step.

Hue	Chroma	CF	RMSE	PSNR
Sample	Sample		0.426	21.41
Mode	Mode		0.304	23.90
Expectation	Expectation		0.374	23.13
Expectation	Expectation	Yes	0.307	24.35
Expectation	Median		0.342	23.77
Expectation	Median	Yes	0.299	24.45

Table 5: **ImageNet/cval1k.** Comparison of various histogram inference methods for hue/chroma. Mode/mode does fairly well but has severe visual artifacts. (CF = Chromatic fading)

B Supplementary results

B.1 Validation

A more detailed list of validation results for hue/chroma inference methods is seen in Table 5.

B.2 Examples

A comparison with Charpiat *et al.* [38] appears in Figures 13 and 14. Examples of how our algorithm can bring old photographs to life in Figure 15. More examples on ImageNet (ctest10k) in Figures 16 to 19 and Figure 20 (failure cases). Examples of histogram predictions in Figures 11 and 12.

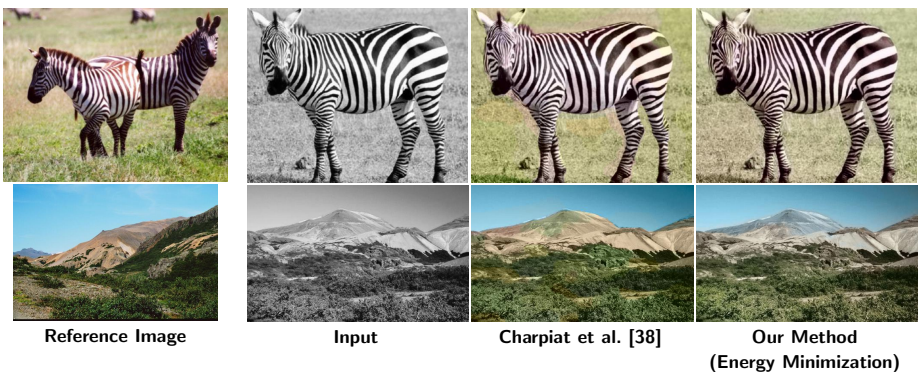


Fig.13: **Transfer.** Comparison with Charpiat *et al.* [38] with reference image. Their method works fairly well when the reference image closely matches (compare with Figure 14). However, they still present sharp unnatural color edges. We apply our histogram transfer method (Energy Minimization) using the reference image.



Fig. 14: **Portraits.** Comparison with Charpiat *et al.* [38], a transfer-based method using 53 reference portrait paintings. Note that their method works significantly worse when the reference images are not hand-picked for each grayscale input (compare with Figure 13). Our model was not trained specifically for this task and we used no reference images.

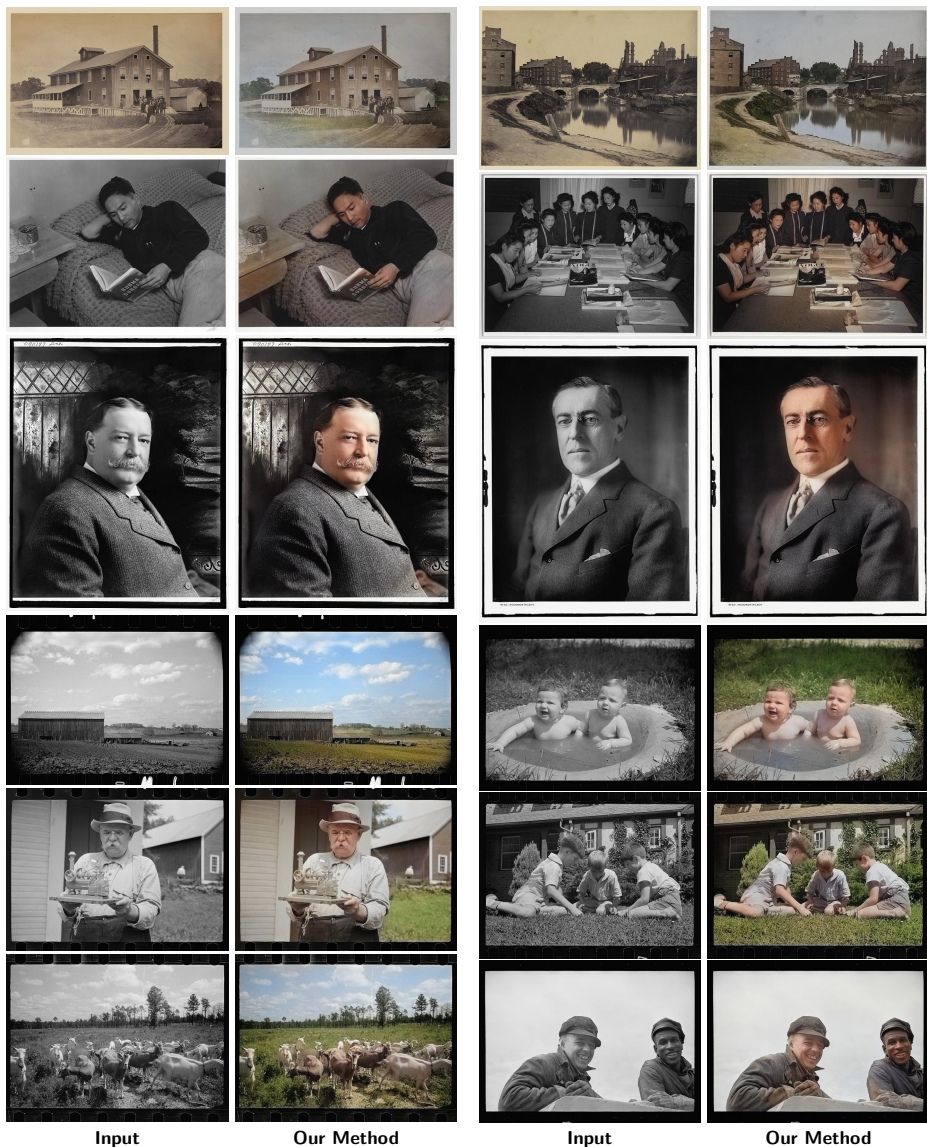


Fig. 15: **B&W photographs.** Old photographs that were automatically colorized.
 (Source: Library of Congress, www.loc.gov)

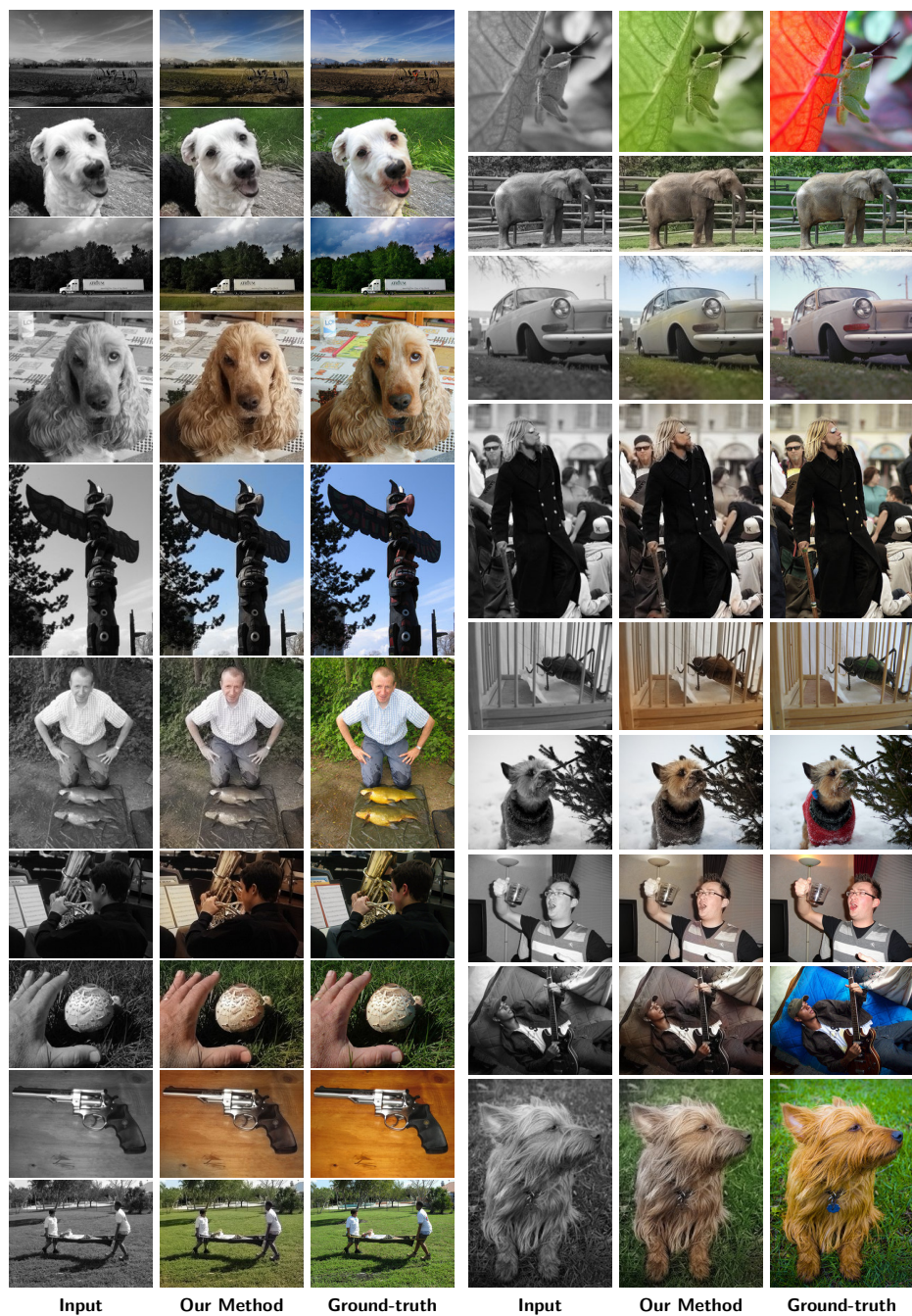


Fig. 16: Fully automatic colorization results on ImageNet/ctest10k.

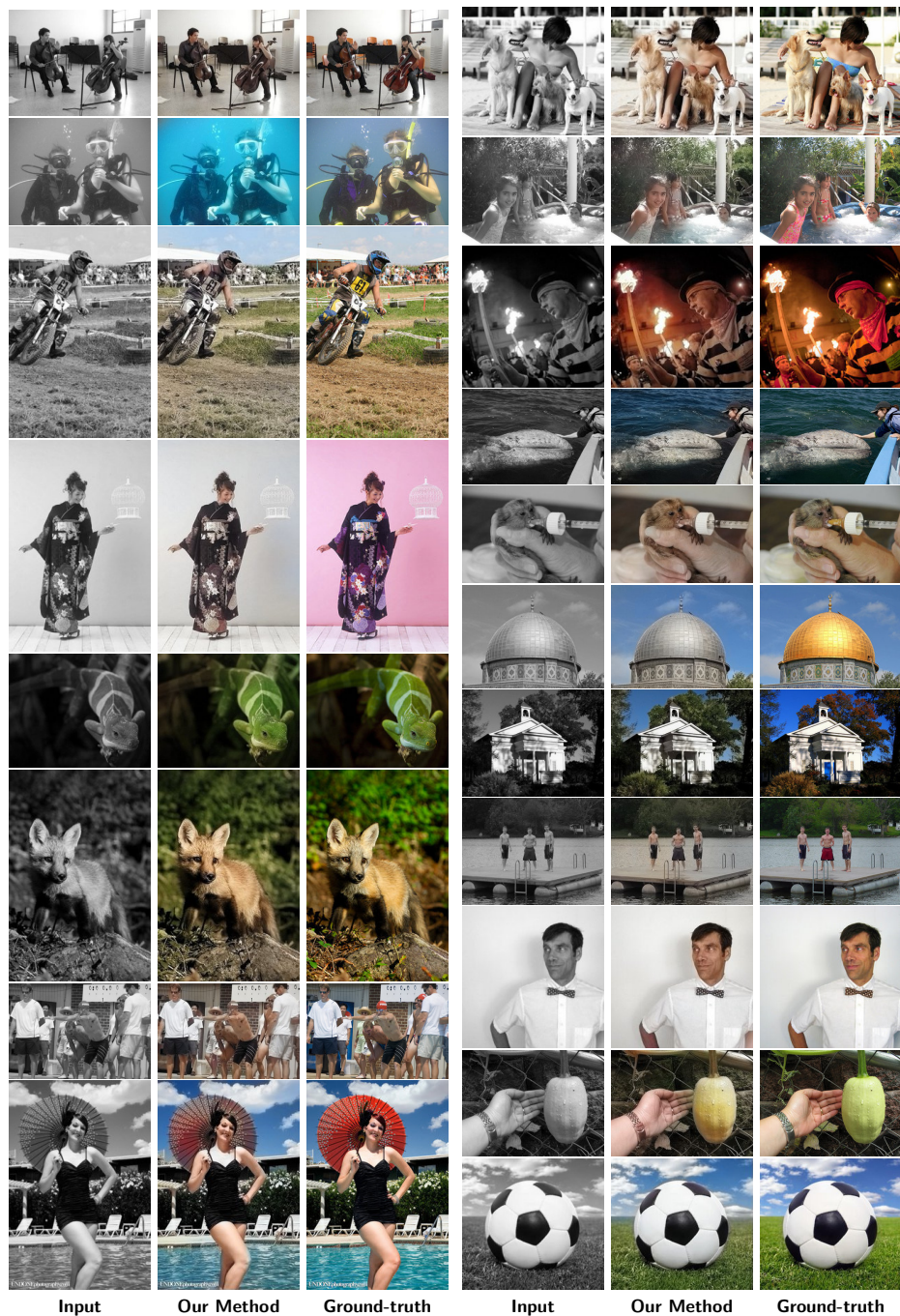


Fig. 17: Fully automatic colorization results on ImageNet/ctest10k.

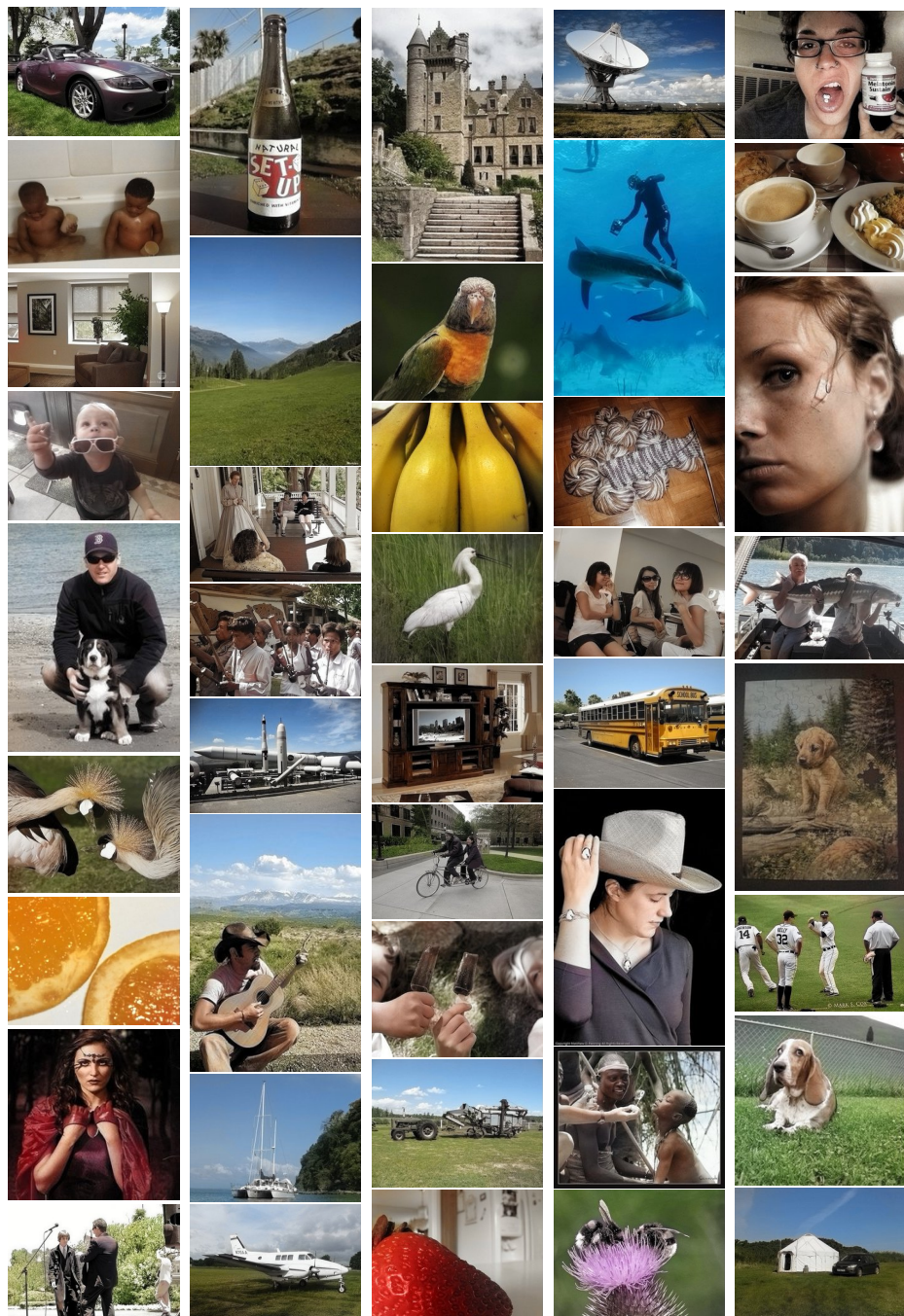


Fig.18: Fully automatic colorization results on ImageNet/ctest10k.



Fig. 19: Fully automatic colorization results on ImageNet/ctest10k.

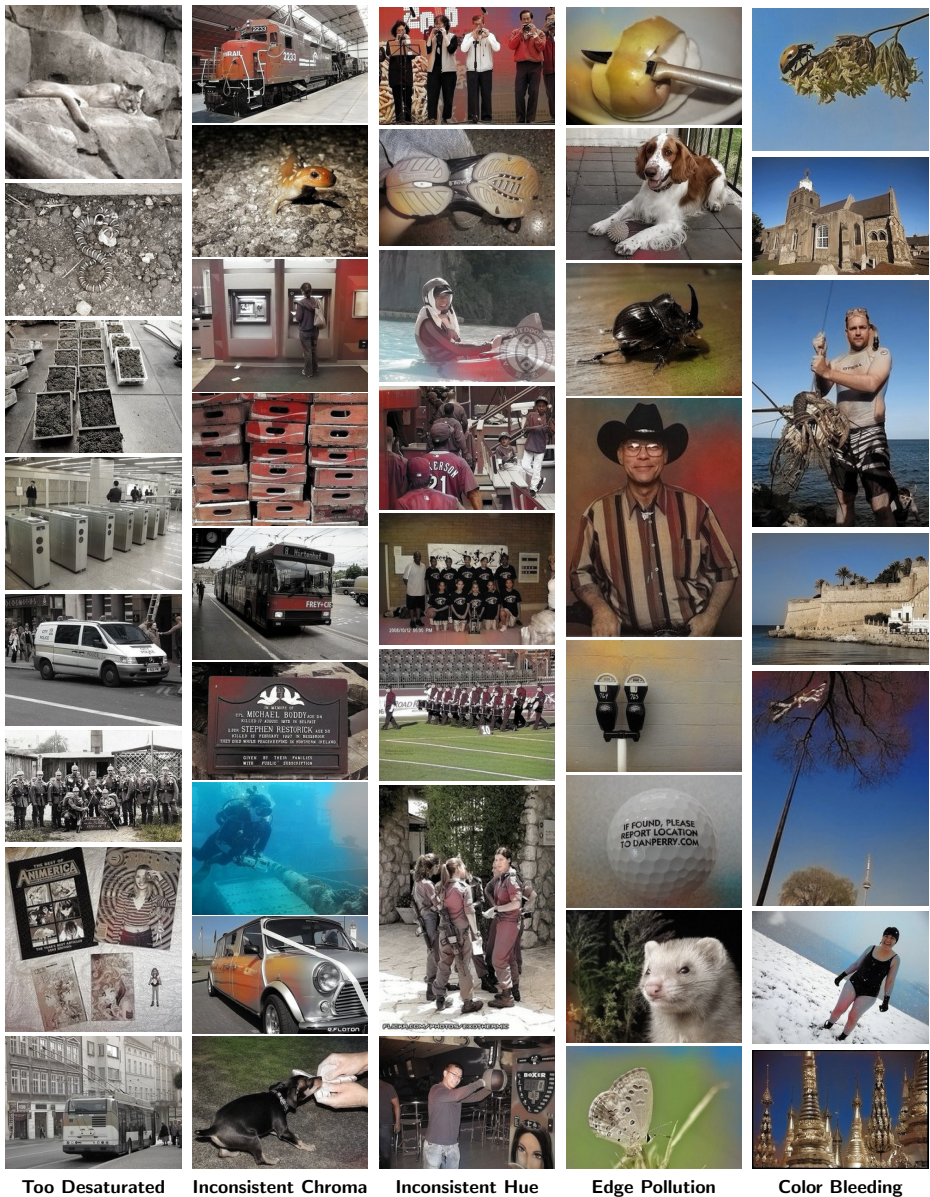


Fig. 20: **Failure cases.** Examples of the five most common failure cases: the whole image lacks saturation (*Too Desaturated*); inconsistent chroma in objects or regions, causing parts to be gray (*Inconsistent Chroma*); inconsistent hue, causing unnatural color shifts that are particularly typical between red and blue (*Inconsistent Hue*); inconsistent hue and chroma around the edge, commonly occurring for closeups where background context is unclear (*Edge Pollution*); color boundary is not clearly separated, causing color bleeding (*Color Bleeding*).